SIAM J. APPL. MATH.
Vol. 63, No. 2, pp. 593–618

THE APEX METHOD IN IMAGE SHARPENING AND THE USE OF LOW EXPONENT LÉVY STABLE LAWS*

ALFRED S. CARASSO†

Abstract. The APEX method is an FFT-based direct blind deconvolution technique that can process complex high resolution imagery in seconds or minutes on current desktop platforms. The method is predicated on a restricted class of shift-invariant blurs that can be expressed as finite convolution products of two-dimensional radially symmetric Lévy stable probability density functions. This class generalizes Gaussian and Lorentzian densities but excludes defocus and motion blurs. Not all images can be enhanced with the APEX method. However, it is shown that the method can be usefully applied to a wide variety of *real blurred images*, including astronomical, Landsat, and aerial images, MRI and PET brain scans, and scanning electron microscope images. APEX processing of these images enhances contrast and sharpens structural detail, leading to noticeable improvements in visual quality. The discussion includes a documented example of nonuniqueness, in which distinct point spread functions produce high-quality restorations of the same blurred image. Significantly, *low exponent* Lévy point spread functions were detected and used in all the above examples. Such low exponents are exceptional in physical applications where symmetric stable laws appear. In the present case, the physical meaning of these Lévy exponents is uncertain.

Key words. image deblurring; blind deconvolution; direct methods; electronic imaging systems; heavy-tailed distributions; low exponent stable laws; APEX method; SECB method; nonuniqueness; astronomical, Landsat, and SEM images; MRI and PET brain scans

AMS subject classifications. 35R25, 35B60, 60E07, 68U10

PII. S0036139901389318

1. Introduction.

The APEX method is an FFT-based direct blind deconvolution technique introduced by the author in [9]. The significance of the present paper lies in the successful use of that method in sharpening a wide variety of *real blurred images*, as opposed to the synthetically blurred images discussed in [9]. The reasons behind these successful applications are not fully understood. Not all images can be usefully enhanced with the APEX method. The present paper is essentially self-contained and may be read independently of [9].

Blind deconvolution seeks to deblur an image without knowing the point spread function (psf) describing the blur. Most approaches to that problem are iterative in nature. Because nonuniqueness is compounded with discontinuous dependence on data, such iterative procedures are not always well-behaved. When the iterative process is stable, several thousand iterations may be necessary to achieve useful reconstructions. However, as shown in [9], by limiting the class of blurs, noniterative direct procedures can be devised that accomplish blind deconvolution of 512×512 images in seconds on current desktop platforms.

The APEX method assumes the image $g(x, y)$ to have been blurred by a restricted type of shift-invariant psf $h(x, y)$, one that can be expressed as a finite convolution

*Received by the editors May 11, 2001; accepted for publication (in revised form) June 5, 2002; published electronically December 11, 2002.

http://www.siam.org/journals/siap/63-2/38931.html

†Mathematical and Computational Sciences Division, National Institute of Standards and Technology, Gaithersburg, MD 20899 (alfred.carasso@nist.gov).

product of two-dimensional (2-D) radially symmetric Lévy stable probability density functions. Such so-called class **G** psfs include Gaussians, Lorentzians, and their convolutions. However, the class **G** also excludes defocus and motion blurs and convolutions of such blurs with Gaussians and Lorentzians.

The synthetically blurred images $g(x, y)$ used in [9] were created by numerical convolution of sharp images $f(x, y)$ with class **G** psfs $h(x, y)$. Such blurred images necessarily obey the convolutional model $g(x, y) = h(x, y) \otimes f(x, y) + noise$, on which the APEX method is predicated. In a real image, the blur need not be radially symmetric nor shift-invariant and may otherwise be poorly approximated by an element of **G**. More fundamentally, the blurring operator may not even be linear. Applicability of the APEX method to a given real image is far from obvious. Therefore, useful sharpening of any such image with an APEX-detected psf is always instructive.

Stable distributions are the natural generalization of the Gaussian distribution. Their theory was developed by Paul Lévy in the 1930s in connection with his work on the central limit theorem (see [17]). In the simplest radially symmetric case, these distributions are characterized by an exponent β, $0 < \beta \leq 1$, with $\beta = 1$ corresponding to the Gaussian distribution, and $\beta = 1/2$ corresponding to the Cauchy or Lorentzian distribution. Because stable distributions have infinite variance when $\beta < 1$, their appearance in physical contexts sometimes poses philosophical difficulties. In the present case, use of such heavy-tailed psfs as the framework for the APEX method is motivated by the important role Lévy densities appear to play in numerous imaging systems. This is documented in section 2. When the APEX method is applied to a given image in the manner described below, a Lévy psf with a specific value of β is necessarily detected. That value of β may not be indicative of the actual physical process that created the image. This is true even if deblurring with the detected psf significantly improves the image. As shown in section 4, there are in general infinitely many distinct values of β that can produce useful reconstructions from the same blurred image. In some cases, the usefully enhanced image may not have been blurred by a class **G** psf to begin with. In other cases, APEX processing does not significantly improve the image.

Below, we exhibit ten images where APEX processing provided noticeable improvement. These examples encompass such diverse imaging applications as astronomical, Landsat, and aerial images, MRI and PET brain scans, a scanning electron microscope image, a face image, and other types of interesting images. In some cases, the improvement is due primarily to an increase in contrast. In other cases, there is demonstrable sharpening of structural detail in addition to increased contrast. In all cases, the change in image quality is more than cosmetic, as APEX processing significantly alters the image Fourier transform. It is noteworthy that *low exponent* stable laws, with $\beta \ll 1/2$, were detected and used to deblur all of the images shown below. Such β-values are exceptional in physical contexts where radially symmetric Lévy densities appear. Whether or not these values have a physical origin cannot be ascertained in the present case. Moreover, the APEX detection procedure may not be well founded. Nevertheless, the fact remains that the use of such psfs produced valuable restoration of real imagery from important fields of science and technology. To the author's knowledge, this application of sub-Cauchy stable laws in image processing is new and unanticipated.

In recent years, there has been considerable interest in image processing techniques that can be formulated as initial value problems in nonlinear PDEs. An instructive survey of these developments may be found in [11]. In particular, novel approaches to image deblurring have been devised, based on integrating well-posed

nonlinear anisotropic diffusion equations [33], [38]. In contrast, the APEX method centers around ill-posed continuation in linear fractional diffusion equations. As noted in section 7, for the type of finely textured imagery considered in the present paper, APEX processing compares favorably with what is feasible with nonlinear methods. This indicates that the APEX method can be a useful addition to PDE-based image analysis.

2. Imaging systems, Lévy processes, and the class G. The occurrence and analysis of Lévy processes in the physical sciences are subjects of significant current interest; see [1], [2], [4], [32], [39], [40], [41], [44], and the references therein. An important special case involves 2-D radially symmetric Lévy stable densities $h(x, y)$, implicitly defined in terms of their Fourier transforms by

$$\hat{h}(\xi,\eta) \equiv \int_{R^2} h(x,y) e^{-2\pi i(\xi x+\eta y)} dxdy = e^{-\alpha(\xi^2+\eta^2)^\beta}, \qquad \alpha > 0, \quad 0 < \beta \leq 1. \tag{1}$$

The cases $\beta = 1$ and $\beta = 1/2$ correspond to Gaussian and Lorentzian (or Cauchy) densities, respectively. For other values of β, $h(x, y)$ in (1) is not known in closed form. When $\beta = 1$, $h(x, y)$ has slim tails and finite variance. For $0 < \beta < 1$, $h(x, y)$ has fat tails and infinite variance. As noted in [44], there are examples in science where the occurrence of a stable law can be deduced from "first principles" in terms of physical mechanisms that do not explicitly involve the parameter β. One such instance is the Holtsmark distribution describing the gravitational field of stars (see [17]). There, mathematical analysis reveals the value $\beta = 3/4$. Such cases must be distinguished from the many other cases in which empirically obtained data with fat tails are *fitted* to a Lévy law, and the exponent β is *inferred* from these data. Given the limitations of physical measurements, such empirically established Lévy processes do not have the degree of scientific legitimacy that attends the Holtsmark distribution. The considerations of the present paper generally lie in this weaker scientific realm. Nevertheless, as will be seen below, techniques derived from such considerations turn out to be effective.

Image intensifiers, charge-coupled devices, and numerous other electronic devices are used in a wide variety of astronomical, industrial, biomedical, military, and surveillance imaging systems; see [3], [14], [15], [18], [31]. Each such device has a psf $h(x, y)$ characterizing that device's imaging properties. The psf is a probability density function since it is nonnegative and integrates to unity. Use of such a device to image an object $f(x, y)$ produces a blurred image $g(x, y) = h(x, y) \otimes f(x, y)$, where $\otimes$ denotes convolution. An ideal device would have $h(x, y) = \delta(x, y)$. The Fourier transform $\hat{h}(\xi, \eta)$ of the psf is generally complex-valued and is called the *optical transfer function* (otf). The absolute value of the otf is the *modulation transfer function* (mtf).

In [42], it is noted that electron optical mtfs are often nearly Gaussian in shape, and that this should be expected from the central limit theorem, since the process of converting incoming signal photons into the final image that is observed on a screen involves many intermediate stages. However, it is also observed in [42] that when such mtfs are fitted with Gaussians, the fitted curves often have *slimmer* tails than is the case for the true mtfs.

A systematic study of electron optical mtf *measurements* is the subject of [22], [24], and [27]. There, the author claims the empirical discovery that a wide variety of electronic imaging devices, including phosphor screens and some types of photographic film, have otfs $\hat{h}(\xi, \eta)$ that are well described by (1) with $1/2 \leq \beta \leq 1$. For any given device, the values of α and β can be determined using specialized graph paper [28].

Other instances of electron optical stable laws are mentioned in [23], [26], and [30]. Analysis of the physical mechanisms responsible for such non-Gaussian behavior is not included in these works. An understanding of such mechanisms may lead to the design of imaging devices with *low* values of β. The latter parameter affects the attenuation of high frequency information in the recorded image. Deconvolution of that image in the presence of noise is generally better behaved at low values of β than it is at high values of β.

The characterization (1) is useful in other areas of optics. The otf for long-exposure imaging through atmospheric turbulence [21] is known to be given by (1), with $\beta = 5/6$ and α determined by atmospheric conditions. Also, as shown in [25], the analytically known diffraction-limited otf for a perfect lens [43, p. 154] can be approximated over a wide frequency range by (1), with $\beta = 3/4$ and α a properly chosen function of the cutoff frequency.

The range of β values discussed above, namely, $1/2 \leq \beta \leq 1$, mirrors that found in most other physical contexts where *symmetric* stable laws appear or are surmised. Values of $\beta \ll 1/2$ seem to be relatively rare in applications. Examples of such β values occur in [29], where mtf data for 56 different kinds of *photographic film* are analyzed. Good agreement is found when these data are fitted with (1) and the pairs (α, β) characterizing each of these 56 mtfs are identified. It is found that 36 types of film have mtfs where $1/2 \leq \beta \leq 1$. The remaining 20 types have mtfs with values of β in the range $0.265 \leq \beta \leq 0.475$.

We now consider imaging systems composed of various elements satisfying (1). Such systems might be used to image objects through a turbulent atmosphere or through other distorting media whose otfs obey (1). The resulting composite otf has the form

$$\hat{h}(\xi,\eta) = e^{-\sum_{i=1}^{J} \alpha_i (\xi^2+\eta^2)^{\beta_i}}, \qquad \alpha_i \geq 0, \quad 0 < \beta_i \leq 1. \tag{2}$$

Such an object corresponds to a *multifractal law* in [4]. We define the class **G** to be the class of all psfs $h(x,y)$ with Fourier transforms satisfying (2). We shall be interested in image deblurring problems

$$Hf \equiv \int_{R^2} h(x-u, y-v) f(u,v) du dv \equiv h(x,y) \otimes f(x,y) = g(x,y), \tag{3}$$

where $g(x,y)$ is the recorded blurred image, $f(x,y)$ is the desired unblurred image, and $h(x,y)$ is a known psf in class **G**. The blurred image $g(x,y)$ includes (possibly multiplicative) noise, which is viewed as a separate additional degradation,

$$g(x,y) = g_e(x,y) + n(x,y). \tag{4}$$

Here, $g_e(x,y)$ is the blurred image that would have been recorded in the absence of any noise, and $n(x,y)$ represents the cumulative effects of all errors affecting final acquisition of the digitized array $g(x,y)$. Neither $g_e(x,y)$ nor $n(x,y)$ are known, only their sum $g(x,y)$. The unique solution of (3) when the right-hand side is $g_e(x,y)$ is the exact sharp image denoted by $f_e(x,y)$. Thus

$$h(x,y) \otimes f_e(x,y) = g_e(x,y). \tag{5}$$

3. Deblurring with the SECB method. The SECB method is a direct FFT-based image deblurring technique designed for equations of the form (3), when $h(x,y)$ is known and belongs to **G**. The method is based on inverse diffusion equations, and

features an important new *slow evolution* regularizing constraint. Such regularization leads to smaller error bounds for the reconstructed image $f(x,y)$, as a function of the noise level ϵ in the blurred image $g(x,y)$, than is mathematically possible with the basic Tikhonov–Miller method. Significantly, the method does not impose smoothness constraints on the unknown image $f(x,y)$, nor does it require knowledge of the noise statistics other than an L^2 upper bound ϵ. Naturally, the method works best when ϵ is small. The above important theoretical advantages, coupled with the practical advantages of fast computation through FFT algorithms, render the SECB method a valuable tool in blind deconvolution. Theoretical analysis of the SECB method, along with error bounds and documented comparisons with the Tikhonov–Miller method, may be found in [5] and [6]. Comparisons with other widely used nonlinear probabilistic algorithms, including the Lucy–Richardson and maximum entropy methods, may be found in [7]. Image deblurring with class **G** psfs is just one example of an extensive class of ill-posed PDE problems [8]. That class includes problems ranging from analytic continuation in the unit disc to the time-reversed Navier–Stokes equations. As shown explicitly in [8], use of the "slow evolution" constraint in that class of problems leads to stronger stability estimates in terms of ϵ than previously known "Hölder-continuity" estimates.

For class **G** psfs, we may define fractional powers H^t, $0 \le t \le 1$, of the convolution integral operator H in (3) as follows:

$$H^t f \equiv \mathcal{F}^{-1}\left\{\hat{h}^t(\xi,\eta)\hat{f}(\xi,\eta)\right\}, \qquad 0 \le t \le 1. \tag{6}$$

Class **G** psfs are intimately related to diffusion processes, and solving (3) is mathematically equivalent to finding the initial value $u(x,y,0) = f(x,y)$ in the *backwards-in-time* problem for the generalized diffusion equation

$$\begin{aligned} &u_t = -\sum_{i=1}^{J} \lambda_i (-\Delta)^{\beta_i} u, \quad \lambda_i = \alpha_i (4\pi^2)^{-\beta_i}, \qquad 0 < t \le 1, \\ &u(x,y,1) \approx g(x,y). \end{aligned} \tag{7}$$

When $f(x,y)$ is known, $u(x,y,t) = H^t f$ is the solution of (7) at time t. The SECB method is a regularization method for solving the ill-posed problem (7) that takes into account the presence of noise in the blurred image data $g(x,y)$ at $t = 1$. With f, g, and n as in (3) and (4), and $u(t)$ the solution of (7), let ϵ, M be known positive constants such that

$$\|u(0)\|_2 = \|f\|_2 \le M, \quad \|u(1) - g\|_2 = \|n\|_2 \le \epsilon, \qquad \epsilon \ll M, \tag{8}$$

where $\|\ \|_2$ denotes the L^2 norm. For any constant $K > 0$ such that $K \ll M/\epsilon$, define $s^*\ (\epsilon, M, K)$ by

$$s^* = \frac{\log\{M/(M - K\epsilon)\}}{\log(M/\epsilon)}. \tag{9}$$

The "slow evolution" constraint applied to the backwards-in-time solution of (7) requires that there exist a known small constant $K > 0$ and a known fixed small $s > 0$, with $s/s^* \gg 1$, such that

$$\|u(s) - u(0)\|_2 \le K\epsilon. \tag{10}$$

Knowledge of the regularization parameters K and s represents a priori information about the solution of (3). As is well known, some form of a priori information is *always* necessary in the solution of ill-posed problems. Given K and s, the SECB solution of the backwards problem for (7) is defined to be that initial value $u^\dagger(0)$ which *minimizes*

$$\|u(1) - g\|_2^2 + K^{-2} \|u(s) - u(0)\|_2^2 \tag{11}$$

over all choices of initial values $u(0)$ in L^2. The SECB deblurred image $f^\dagger(x,y) \equiv u^\dagger(0)$ can be obtained in closed form in Fourier space. With $\overline{z}$ denoting the complex conjugate of z,

$$\hat{f}^\dagger(\xi,\eta) = \frac{\overline{\hat{h}}(\xi,\eta)\hat{g}(\xi,\eta)}{|\hat{h}(\xi,\eta)|^2 + K^{-2}|1 - \hat{h}^s(\xi,\eta)|^2}, \tag{12}$$

leading to $f^\dagger(x,y)$ upon inverse transformation. In practice, FFT algorithms are used to obtain $f^\dagger(x,y)$. This may result in individual pixel values that are negative or that exceed 255, the maximum value in an 8-bit image. Accordingly, all negative values are reset to the value zero, and all values exceeding 255 are reset to the value 255. One way of obtaining initial estimates for K and s in (12) is as follows. With ϵ, M, and the psf $h(x,y)$ known, fix $s > 0$ in the range $0.001 \le s \le 0.01$ and construct the operator H^s as in (6). If $f^\pi(x,y)$ is a prototype image for the class of images under consideration, we can estimate K in (10) by evaluating $\|H^s f^\pi - f^\pi\| / \epsilon$. We may then compute s^* in (9) and verify that $s/s^* \gg 1$. This is usually the case, as s^* is infinitesimally small, provided that $K\epsilon \ll M$. This initial choice of K can be refined interactively when the reconstructed image is a recognizable object. With s fixed as above, increasing K increases resolution until a threshold value is reached. Further increases in K bring out noise. Conversely, if the initial choice of K brings out noise, K must be decreased. Note that for 512×512 images, 20 trial SECB restorations, each with a different value of K, can be obtained simultaneously in about 10 seconds of cpu time on an MIPS R12000 (400MHz) workstation. A visually optimal value of K for fixed small s is usually easily found. We may also form and display

$$u^\dagger(x,y,t) = H^t f^\dagger(x,y) \tag{13}$$

for selected *decreasing* values of t lying between 1 and 0. This simulates *marching backwards in time* in (7) and allows *monitoring* the gradual deblurring of the image. As $t \downarrow 0$, the partial restorations $u^\dagger(x,y,t)$ become sharper. However, noise and other artifacts typically become more noticeable as $t \downarrow 0$. Marching backwards from $t = 0.2$ to $t = 0$, say, may allow detection of features in the image before they become obscured by noise or ringing artifacts.

The above discussion assumed that the psf $h(x,y)$ was known. As shown in sections 5 and 6, such marching backwards in time becomes much more vital in the blind deconvolution problem, where the initial APEX-detected psf may erroneously be *too wide*. Theoretically, use of too wide a psf all the way to $t = 0$ implies sharpening features that may have already become infinitely sharp at some $t_0 > 0$. In practice, this leads to severe ringing and other undesirable artifacts at $t = 0$. Here, it is often advisable to start marching backwards from $t = 1$.

It should be noted that the class **G** is only a small subclass of the class of *infinitely divisible* densities [17]. The latter class includes multimodal nonsymmetric psfs associated with linear diffusion equations more complex than (7). Detection of

such psfs from blurred image data would require considerable extension of the APEX method discussed below.

4. Nonuniqueness in blind deconvolution. Blind deconvolution of images is a mathematical problem that is not fully understood. Well-documented examples of the kinds of behavior that may occur are of particular interest. In this section, we highlight important nonuniqueness aspects of that problem that are helpful in understanding the results of the APEX method. Let $f_e(x,y)$ be a given exact sharp image, let $h(x,y)$ be a Lévy point spread function, and let $g_e(x,y) = h(x,y) \otimes f_e(x,y)$. We shall show that, given the blurred image $g_e(x,y)$, there are in general *many* point spread functions $h_i(x,y) \neq h(x,y)$ that deblur $g_e(x,y)$, producing *high quality* reconstructions $f_i(x,y) \neq f_e(x,y)$, with $h_i(x,y) \otimes f_i(x,y) \approx g_e(x,y)$.

The sharp 512×512 Sydney image $f_e(x,y)$ in Figure 1(a) was synthetically blurred by convolution with a Cauchy density $h(x,y)$ with $\alpha_0 = 0.075$, $\beta_0 = 0.5$. This produced the blurred image $g_e(x,y)$ in Figure 1(b). To avoid distractions caused by noise, the blurred image $g_e(x,y)$ in this experiment was computed and stored in 64-bit precision. Deblurring this noiseless image with the correct psf values $\alpha = 0.075$, $\beta = 0.5$, produces Figure 1(c). This is in excellent visual agreement with $f_e(x,y)$ in Figure 1(a), as expected. However, the visual quality in Figures 1(d)–(f) is generally as good as that in Figure 1(c); the latter three images were deblurred with Lévy densities with values (α,β), where $\alpha > \alpha_0$, $\beta < \beta_0$, and they differ from Figure 1(a) in contrast and brightness. All deblurred images were obtained using the SECB method with $s = 0.001$ and $K = 10000$. One-dimensional (1-D) cross sections of the four distinct psfs used in Figure 1 are displayed in Figure 2. These psfs also exhibit distinct heavy tail behavior not shown in Figure 2.

One can imagine four photographers, simultaneously photographing the identical scene depicted in Figure 1(a), yet producing the four distinct images shown in Figures 1(c)–(f) through use of different lenses, film, filters, exposures, printing, and the like. In practice, given only the blurred image in Figure 1(b), any one of these four restorations would be considered highly successful. Convolution of each reconstruction with its corresponding psf in Figure 2 reproduces the blurred image in Figure 1(b).

For any restoration $f(x,y)$ of the exact image $f_e(x,y)$ in Figure 1(a) and any norm $\|\ \|$, we can evaluate the relative error $\|f - f_e\| / \|f_e\|$. Define the discrete L^1, L^2, and H^m norms as follows:

$$\|f\|_1 = N^{-2} \sum_{x,y=1}^{N} |f(x,y)|,$$

$$\|f\|_2 = \left\{ N^{-2} \sum_{x,y=1}^{N} |f(x,y)|^2 \right\}^{1/2}, \tag{14}$$

$$\|f\|_{H^m} = \left\{ N^{-2} \sum_{\xi,\eta=1}^{N} \left(1 + \xi^2 + \eta^2\right)^m |\hat{f}(\xi,\eta)|^2 \right\}^{1/2}.$$

The relative errors in the L^1, L^2, H^1, and H^5 norms for each of the four restorations in Figure 1 are shown in Table 1. As might be expected, image (c) is the closest to image (a) in each of these norms, since the correct psf values were used to obtain image (c) from image (b). It is also evident from Table 1 that the four restorations are distinct from one another, since they differ from image (a) by different amounts.

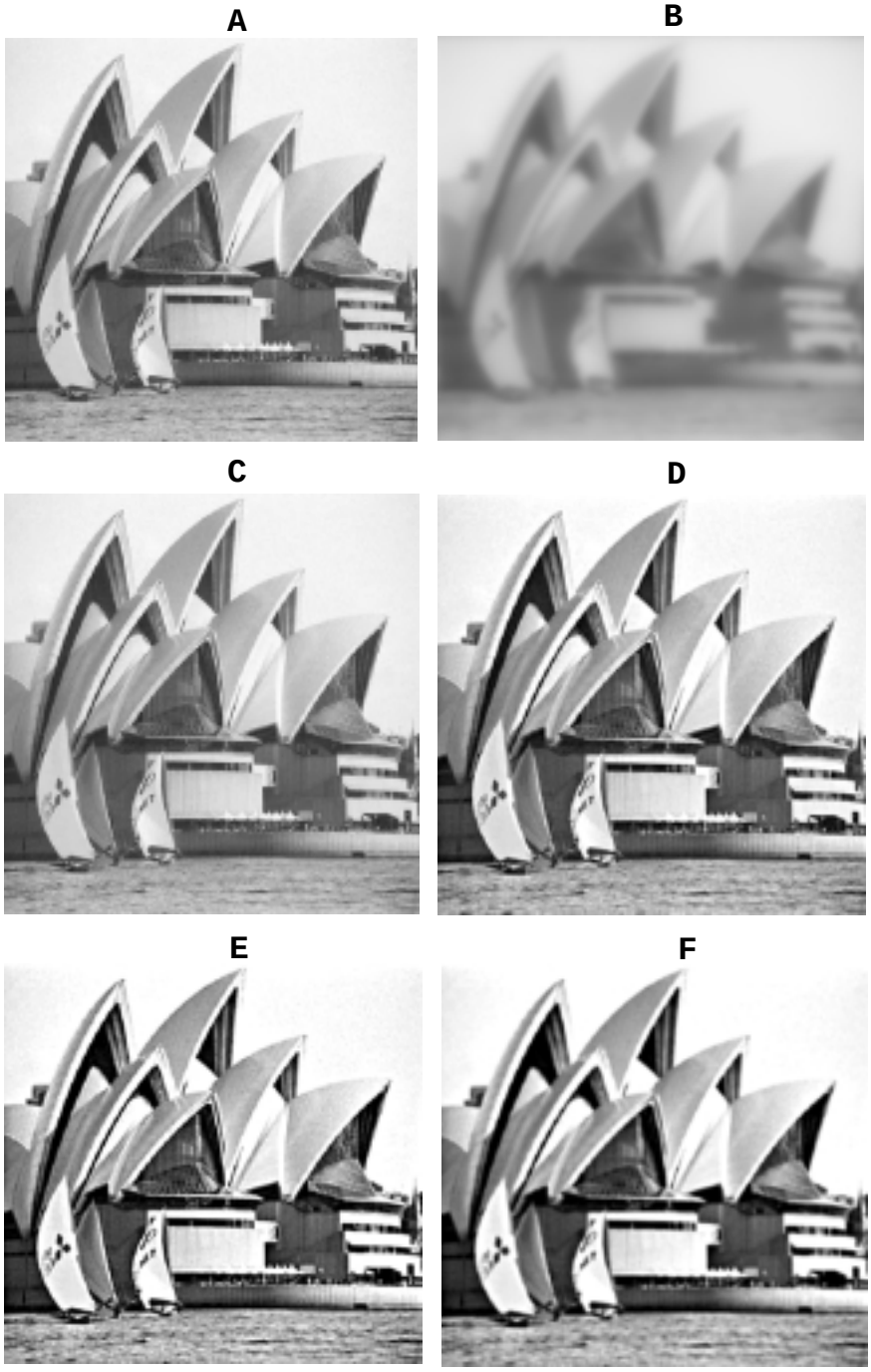

FIG. 1. *Nonuniqueness in blind deconvolution. Distinct psfs exist that produce high quality reconstructions from the same blurred image.* (a) *Original sharp* 512×512 *Sydney image.* (b) *Synthetically blurred Sydney image created by convolution with Lorentzian density with* $\alpha_0 = 0.075$, $\beta_0 = 0.5$. *Blurred image computed and stored in* 64*-bit precision.* (c) *Deblurring of image* (b) *using correct parameters* $\alpha = 0.075$, $\beta = 0.5$. (d) *Deblurring of image* (b) *using* $\alpha = 0.1301264$, $\beta = 0.44298$. (e) *Deblurring of image* (b) *using* $\alpha = 0.1950345$, $\beta = 0.403889$. (f) *Deblurring of image* (b) *using* $\alpha = 0.2360994$, $\beta = 0.369666$. *Notice that images* (d), (e), *and* (f) *were found using specific pairs* (α, β), *where* $\alpha > \alpha_0$ *and* $\beta < \beta_0$. *All deblurred images were obtained using the SECB procedure with* $s = 0.001$ *and* $K = 10000$.

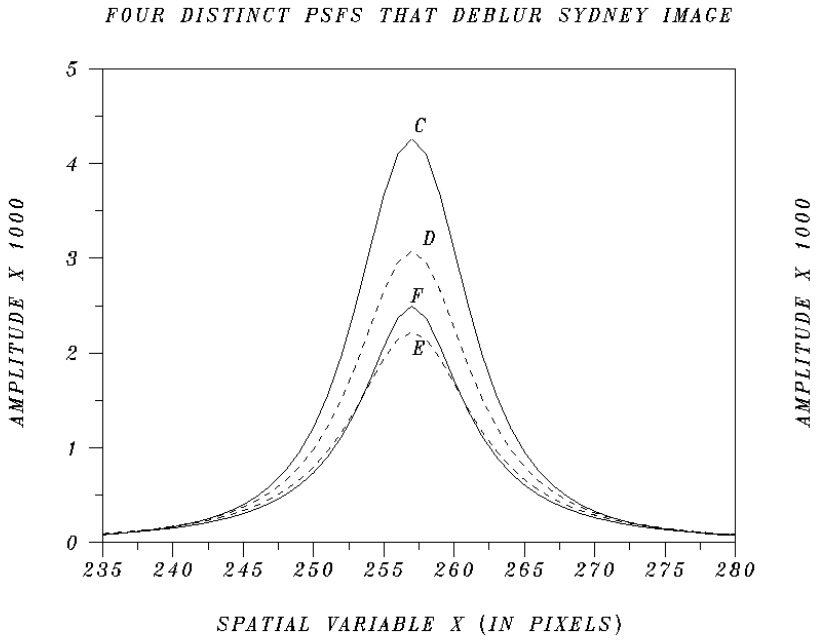

FIG. 2. *Four distinct psfs that deblur image* (b) *in Figure* 1. *Curves C, D, E, and F are* 1-*D cross sections of the* 512×512 *psfs that respectively produced images* (c), (d), (e), *and* (f) *in Figure* 1. *These psfs also exhibit distinct heavy tail behavior.*

TABLE 1
Relative errors in various norms for the four deblurred images in Figure 1.

Restoration	*Parameters* $\alpha,\ \beta$	L^1	L^2	H^1	H^5
Image (c)	$\alpha = 0.075,\ \beta = 0.500$	2.13 %	3.52 %	4.13 %	19.66 %
Image (d)	$\alpha = 0.130,\ \beta = 0.443$	6.63 %	8.37 %	8.67 %	21.11 %
Image (e)	$\alpha = 0.195,\ \beta = 0.404$	12.64 %	15.53 %	15.75 %	25.52 %
Image (f)	$\alpha = 0.236,\ \beta = 0.370$	12.54 %	15.08 %	15.31 %	26.17 %

Most important, the fact that image (e) is a significantly poorer approximation to image (a) in these norms than is image (c) *does not imply* that image (e) is an inaccurate representation of the visual scene depicted in image (a). Notice also that image (f) is not as sharp as image (e), although it is closer to image (a) in three of the four norms.

Iterative algorithms are the most common approach to blind deconvolution. Convergence proofs for such iterative procedures are seldom available. The above example illustrates some of the difficulties underlying any analysis of convergence. Such analysis should allow for the possibility of *infinitely many* useful limit points, while the mathematical characterization of such limit points is not obvious. Moreover, as is evident from Table 1 and has been known for some time, the use of L^p or H^m norms in assessing the visual quality of a reconstruction can be misleading.

5. Marching backwards in time and the APEX method. The APEX method is a blind deconvolution technique based on detecting class **G** psf signatures by appropriate 1-D Fourier analysis of the blurred image $g(x, y)$. The detected

psf parameters are then input into the SECB algorithm to deblur the image. Let $f_e(x,y)$ be an exact sharp image as in (5). Since $f_e(x,y) \geq 0$,

$$|\hat{f}_e(\xi,\eta)| \leq \int_{R^2} f_e(x,y)dxdy = \hat{f}_e(0,0) = \sigma > 0. \tag{15}$$

Also, since $g_e(x,y) = h(x,y) \otimes f_e(x,y)$ and $h(x,y)$ is a probability density,

$$\hat{g_e}(0,0) = \int_{R^2} g_e(x,y)dxdy = \int_{R^2} f_e(x,y)dxdy = \hat{f}_e(0,0) = \sigma > 0. \tag{16}$$

Using σ as a normalizing constant, we may normalize Fourier transform quantities $\hat{q}(\xi,\eta)$ by dividing by σ. Let

$$\hat{q}^*(\xi,\eta) = \frac{\hat{q}(\xi,\eta)}{\sigma} \tag{17}$$

denote the normalized quantity. The function $|\hat{f_e}^*(\xi,\eta)|$ is highly oscillatory, and $0 \leq |\hat{f_e}^*| \leq 1$. Since $f_e(x,y)$ is real, its Fourier transform is conjugate symmetric. Therefore, the function $|\hat{f_e}^*(\xi,\eta)|$ is symmetric about the origin on any line through the origin in the (ξ,η) plane. The same is true for the blurred image data $|\hat{g}^*(\xi,\eta)|$.

All blurred images in this and the next section are of size 512×512 and quantized at 8 bits per pixel. For any blurred image $g(x,y)$, the discrete Fourier transform is a 512×512 array of complex numbers, which we again denote by $\hat{g}(\xi,\eta)$ for simplicity. The "frequencies" ξ,η are now integers lying between -256 and 256, and the zero frequency is at the center of the transform array. This ordering is achieved by premultiplying $g(x,y)$ by $(-1)^{x+y}$. We shall be interested in the values of such transforms along single lines through the origin. The discrete transforms $|\hat{g}^*(\xi,0)|$ and $|\hat{g}^*(0,\eta)|$ are immediately available. Image rotation may be used to obtain discrete transforms along other directions. All 1-D Fourier domain plots shown in this paper are taken along the axis $\eta = 0$ in the (ξ,η) plane. In these plots, the zero frequency is at the center of the horizontal axis, and the graphs are necessarily symmetric about the vertical line $\xi = 0$. Examples of such plots are shown in Figures 3, 5, and 10.

The class of blurred images $g(x,y)$ considered in the present paper can be described in terms of the behavior of $\log|\hat{g}^*(\xi,\eta)|$ along lines through the origin in the (ξ,η) plane. While local behavior is highly oscillatory, global behavior is generally monotone decreasing and *convex*. This is shown in Figure 3 for two typical images along the line $\eta = 0$. In [9], a large class of images with that property was exhibited, the class **W**. The blurred images considered here may be loosely characterized as being in class **W**. Not all blurred images may be so characterized. For example, if the Cindy Crawford image $g(x,y)$ in Figure 3(a) were convolved with a wide Gaussian psf to form a new blurred image $g_1(x,y)$, global behavior in $\log|\hat{g_1}^*(\xi,0)|$, away from the origin, would be monotone decreasing and *concave*. Application of the APEX method to several concave examples is discussed in [9]. Convolution of Figure 3(a) with a defocus psf produces a different kind of blurred image $g_2(x,y)$, and global behavior in $\log|\hat{g_2}^*(\xi,0)|$ is neither concave nor convex. Instead, there is a regular pattern of sharp singularities corresponding to successive zeroes of the defocus otf. Use of the APEX method in the manner to be described below is intended only for blurred images with Fourier behavior analogous to that shown in Figure 3.

The APEX method is based on the following observations. In the basic relation

$$g(x,y) = h(x,y) \otimes f_e(x,y) + n(x,y), \tag{18}$$

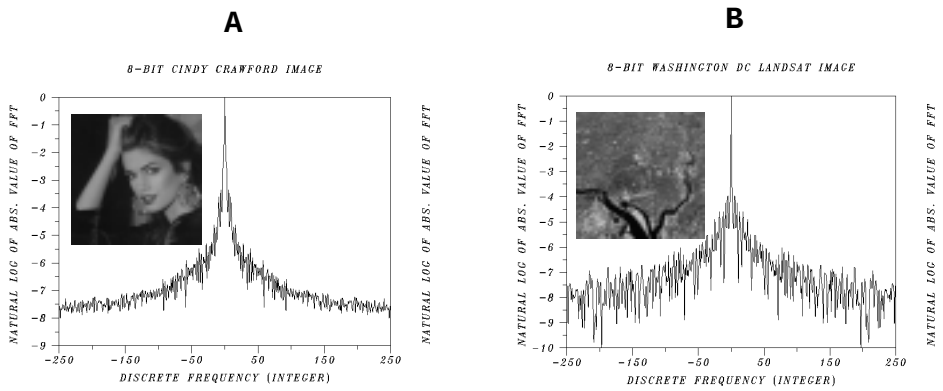

FIG. 3. *Behavior of a normalized Fourier transform in types of blurred images $g(x,y)$ considered in the present paper.* (a) $\log|\hat{g}^*(\xi,0)|$ *in an image of Cindy Crawford.* (b) $\log|\hat{g}^*(\xi,0)|$ *in a Washington, DC Landsat image. While local behavior is highly oscillatory, global behavior is generally monotone decreasing and convex.*

we may safely assume that the noise $n(x,y)$ satisfies

$$\int_{R^2} |n(x,y)|dxdy \ll \int_{R^2} f_e(x,y)dxdy = \sigma > 0, \tag{19}$$

so that

$$|\hat{n}^*(\xi,\eta)| \ll 1. \tag{20}$$

Consider the case in which the otf is a pure Lévy density $\hat{h}(\xi,\eta) = e^{-\alpha(\xi^2+\eta^2)^\beta}$. Since $g = g_e + n$,

$$\log|\hat{g}^*(\xi,\eta)| = \log|e^{-\alpha(\xi^2+\eta^2)^\beta}\hat{f_e}^*(\xi,\eta) + \hat{n}^*(\xi,\eta)|. \tag{21}$$

Let $\Omega = \{(\xi,\eta) \mid \xi^2+\eta^2 \le \omega^2\}$ be a neighborhood of the origin, where

$$e^{-\alpha(\xi^2+\eta^2)^\beta}|\hat{f_e}^*(\xi,\eta)| \gg |\hat{n}^*(\xi,\eta)|. \tag{22}$$

Such an Ω exists since (22) is true for $\xi = \eta = 0$, in view of (20). The radius $\omega > 0$ of Ω decreases as α and n increase. For $(\xi,\eta) \in \Omega$ we have

$$\log|\hat{g}^*(\xi,\eta)| \approx -\alpha(\xi^2+\eta^2)^\beta + \log|\hat{f_e}^*(\xi,\eta)|. \tag{23}$$

Because of the radial symmetry in the psf, it is sufficient to consider (23) along a single line through the origin in the (ξ,η) plane. Choosing the line $\eta = 0$, we have

$$\log|\hat{g}^*(\xi,0)| \approx -\alpha|\xi|^{2\beta} + \log|\hat{f_e}^*(\xi,0)|, \qquad |\xi| \le \omega. \tag{24}$$

Some type of a priori information about $f_e(x,y)$ is necessary for blind deconvolution. In (24), knowledge of $\log|\hat{f_e}^*(\xi,0)|$ on $|\xi| \le \omega$ would immediately yield $\alpha|\xi|^{2\beta}$ on that interval. Moreover, any other line through the origin could have been used in (23). However, such detailed knowledge is unlikely in practice. The APEX method seeks to identify a useful psf from (24) without prior knowledge of $\log|\hat{f_e}^*(\xi,0)|$. The

method assumes instead that $f_e(x,y)$ is a recognizable object, and typically requires several interactive trials before locating a suitable psf. As previously noted, such trial SECB restorations are easily obtained. Here, prior information about $f_e(x,y)$ is disguised in the form of user recognition or rejection of the restored image, and that *constraint* is applied at the end of the reconstruction phase, rather than at the beginning of the detection phase.

In the absence of information about $\log|\hat{f}_e^{\,*}(\xi,0)|$, we replace it by a negative constant $-A$ in (24). For any $A>0$, the approximation

$$\log|\hat{g}^*(\xi,0)| \approx -\alpha|\xi|^{2\beta} - A \tag{25}$$

is not valid near $\xi = 0$, since the curve $u(\xi) = -\alpha|\xi|^{2\beta} - A$ has $-A$ as its apex. Choosing a value of $A>0$, we best fit $\log|\hat{g}^*(\xi,0)|$ with $u(\xi) = -\alpha|\xi|^{2\beta} - A$ on the interval $|\xi| \le \omega$, using nonlinear least squares algorithms. The resulting fit is close only for ξ away from the origin. The returned values for α and β are then used in the SECB deblurring algorithm. Different values of A return different pairs (α,β). Experience indicates that useful values of A generally lie in the interval $2 \le A \le 6$. Increasing the value of A decreases the curvature of $u(\xi)$ at $\xi = 0$, resulting in a larger value of β together with a smaller value of α. A value of $A>0$ that returns $\beta > 1$ is clearly too large, as $\beta > 1$ is impossible for probability density functions [17]. Decreasing A has the opposite effect, producing lower values of β and higher values of α. As a rule, deconvolution is better behaved at lower values of β than it is when $\beta \approx 1$. A significant observation is that *an image blurred with a pair* (α_0,β_0) *can often be successfully deblurred with an appropriate pair* (α,β)*, where* $\alpha > \alpha_0$ *and* $\beta < \beta_0$. Examples of this phenomenon were shown in Figure 1 in connection with the blurred Sydney image. An effective interactive framework for performing the above least squares fitting is the *fit* command in *DATAPLOT* [20]. This is a high-level English-syntax graphics and analysis software package developed at the National Institute of Standards and Technology. This software tool was used throughout this paper.

The following version of the APEX method, using the SECB *marching backwards in time* option (13), has been found useful in a variety of image enhancement problems where the image $g(x,y)$ is such that $\log|\hat{g}^*(\xi,0)|$ is generally globally monotone decreasing and convex, as shown in Figure 3. Choose a value of $A>2$ in (25) such that the least squares fit develops a slight *cusp* at $\xi = 0$. Using the returned pair (α,β) in the SECB method, obtain a sequence $u^\dagger(x,y,t)$ of partial restorations as t decreases from $t=1$, as illustrated in the Cindy Crawford sequence[1] in Figure 4. Often, the initial choice of A results in a psf that is *too wide* in physical space, i.e., wider than the unknown psf that might have blurred the image. Use of that psf all the way to $t=0$ will result in *oversharpening*. Typically, high quality restorations will be found at positive values of t, and these will gradually deteriorate as $t \downarrow 0$. At $t=0$, the restoration may exhibit severe ringing and other undesirable artifacts [9, Figure 13], indicating that continuation backwards in time has proceeded *too far* in (7). Terminating the continuation at some appropriate $t = t_1 > 0$ is equivalent to rescaling the value of α without changing the value of β. If the pair (α,β) produces a high quality restoration at $t = t_1 > 0$, the pair (α_1,β), where $\alpha_1 = (1-t_1)\alpha$, will produce the same quality results at $t=0$. Thus, marching backwards in time is equivalent to simultaneously sampling numerous values of α while keeping β fixed. This process

[1] Given a 512×512 blurred image as input, the APEX procedure computes and displays a time marching sequence of 10 partial restorations in about 10 seconds on an MIPS R12000 (400MHz) workstation.

FIG. 4. *Enhancement of a Cindy Crawford image by marching backwards from $t = 1$ with an APEX-detected psf. Image sequence shows a gradual increase in contrast as t decreases. Undesirable artifacts at $t = 0$ indicate that continuation backwards in time has proceeded too far. Best results are highly subjective in this case, but probably occur at some $t > 0.5$. Note the sharpness of the earrings near $t = 0.5$.*

can be repeated with a different choice of A, resulting in a different value of β. In general, there will be many values of A in (25) returning pairs (α, β) that produce good reconstructions at some $t_{\alpha\beta} > 0$. A large number of distinct pairs (α^*, β^*) can thus be found that produce useful, but distinct, results at $t = 0$. Indeed, this is the process that was used to obtain the four psfs shown in Figure 2.

We have been assuming $\hat{h}(\xi, \eta)$ to be a pure Lévy otf in (18). For more general class **G** otfs (2), we may still use the approximation $\log|\hat{g}^*(\xi, 0)| \approx -\alpha|\xi|^{2\beta} - A$ and apply the same technique to extract a suitable pair (α, β) from the blurred image. Here, the returned APEX values may be considered representative values for the α_i, β_i in (2), producing a single pure Lévy otf approximating the composite otf.

6. Application to real images. The developments in sections 2 through 5 are predicated on two assumptions. The first assumption is that the blurred image $g(x, y)$ obeys the simple convolution equation (3) rather than a more general, possibly nonlinear, integral equation

$$Hf = \int_{R^2} h(x, y, u, v, f(u, v))dudv = g(x, y). \tag{26}$$

In addition to linearity, (3) implies that the blur is isoplanatic. The second assumption is that the point spread function $h(x, y)$ belongs to a restricted class of unimodal, radially symmetric, probability density functions, the class **G** defined in (2). In [9], successful blind deconvolution of *synthetically blurred* images, with added noise, was demonstrated. Such synthetically blurred images necessarily obey (2) and (3).

The applicability of the preceding theory to real blurred images is by no means assured. Deviations from linearity, isoplanatism, unimodality, and radial symmetry

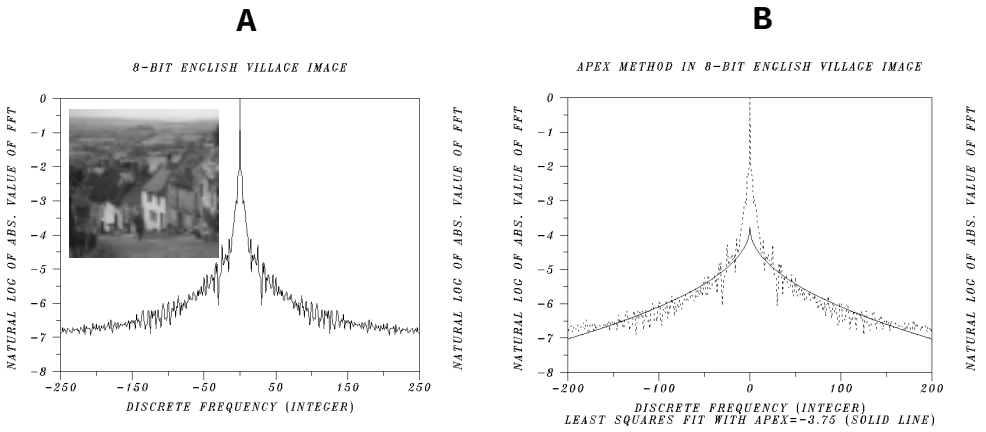

FIG. 5. *The APEX method of psf detection.* (a) $\log|\hat{g}^*(\xi,0)|$ *on* $|\xi| \le 250$ *in the* 8*-bit English village image.* (b) *A least squares fit of* $\log|\hat{g}^*(\xi,0)|$*, with* $u(\xi) = -\alpha\ |\xi|^{2\beta} - 3.75$ *on* $|\xi| \le 200$*, develops a cusp at* $\xi = 0$ *and returns* $\alpha = 0.251274$*,* $\beta = 0.242246$*.*

are possible. Moreover, the class **G** excludes motion and defocus blurs. In addition, the types and intensities of noise processes in real images may differ fundamentally from the noise models typically used in numerical experiments. Therefore, only limited success on a narrow class of images can be expected in real applications.

The examples discussed below involve images obtained from multiple sources using diverse imaging modalities. Some of these images have been used as test images in the literature. In this paper, each of these images is assumed to have been blurred by some unknown process, and we seek to improve visual quality by APEX processing. All images are of size 512×512 and are quantized at 8 bits per pixel.

Our first example is a well-known English village image denoted by $g(x, y)$ and shown in Figure 5(a) together with $\log|\hat{g}^*(\xi,0)|$ on $|\xi| \le 250$. The plot displays globally convex monotone behavior. In Figure 5(b), the APEX fit of $\log|\hat{g}^*(\xi,0)|$ with $u(\xi) = -\alpha|\xi|^{2\beta} - A$ on the interval $|\xi| \le 200$ is shown. With $A = 3.75$, the fit develops a cusp at $\xi = 0$ and returns $\alpha = 0.251274$, $\beta = 0.242246$. With these psf parameters, SECB deblurring using $s = 0.01$, $K = 1300$, and continuation backwards in time terminated at $t = 0.5$ produces Figure 6(b). This is compared with the original in Figure 6(a).

The extent of sharpening in Figure 6(b) becomes evident when zooming in on selected parts of the image. In Figure 7, roof lines on the first three houses are compared before and after APEX processing. There is noticeable enhancement of structural detail in the roof shingles and stone fronts of the three houses in Figure 7(b). In Figure 8(b), Holstein cows grazing in the meadow, not previously identifiable, are clearly visible. So are individual chimney bricks. In Figure 9(b), buildings in the distance, not readily noticed in Figure 9(a), become well defined.

It should be noted that the use of a different value of A, and/or a different neighborhood of the origin Ω in Figure 5(b), may return a different psf pair (α, β). In that case, backwards continuation in the SECB method may need to be terminated at some other value of t to obtain the best image. However, with good choices of A and Ω, the new image would again be a high quality representation of the visual scene in Figure 6(b), while differing from Figure 6(b) at individual pixels. This is

FIG. 6. *Enhancement of the English village image.* (a) *Original* 8*-bit image.* (b) *SECB deblurred image using* $s = 0.01$, $K = 1300$, *with APEX-detected values* $\alpha = 0.251274$, $\beta = 0.242246$, *and with continuation backwards in time terminated at* $t = 0.5$.

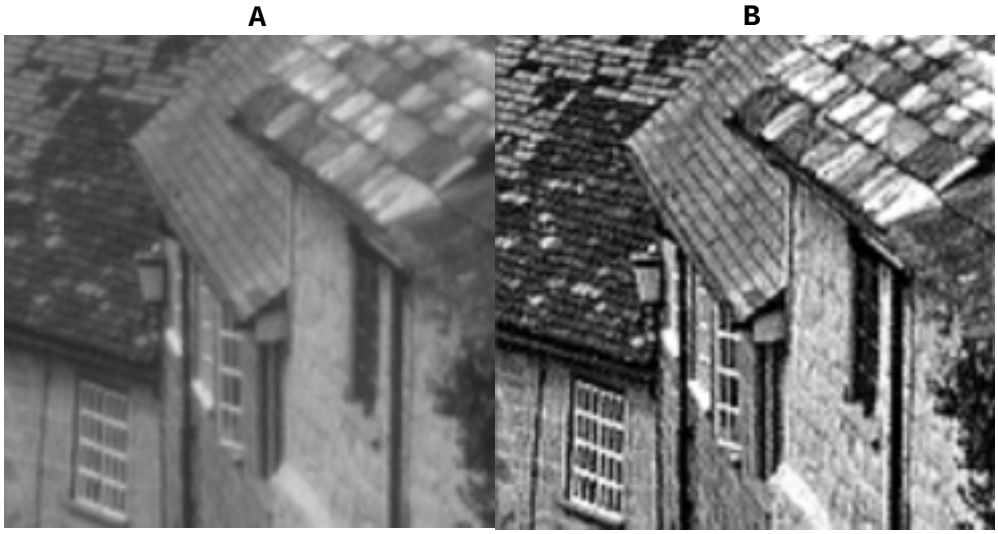

FIG. 7. *Extent of sharpening in the English village scene becomes evident when zooming in on selected parts of the image.* (a) *Roof lines in the original image.* (b) *Roof lines in the enhanced image.*

the nonuniqueness phenomenon previously discussed in connection with the Sydney image in Figure 1.

Deconvolution of Figure 6(a) with the above APEX-detected psf significantly alters its Fourier transform. As shown in Figure 10(a), the Fourier transform in Figure 6(b) (dashed curve) decays less rapidly as $|\xi|$ increases than was the case in the original Figure 6(a) (solid curve). Evidently, APEX processing amplifies high frequency image components in a stable coherent fashion, resulting in the overall

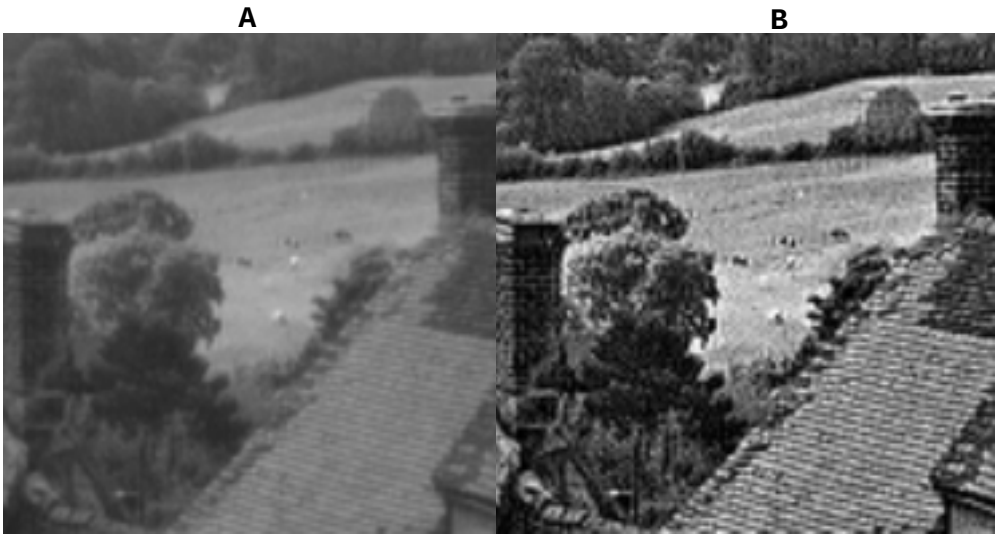

FIG. 8. *Extent of sharpening in the English village scene becomes more evident with zooming. Holstein cows grazing in the meadow in image* (b) *are not readily identifiable in image* (a).

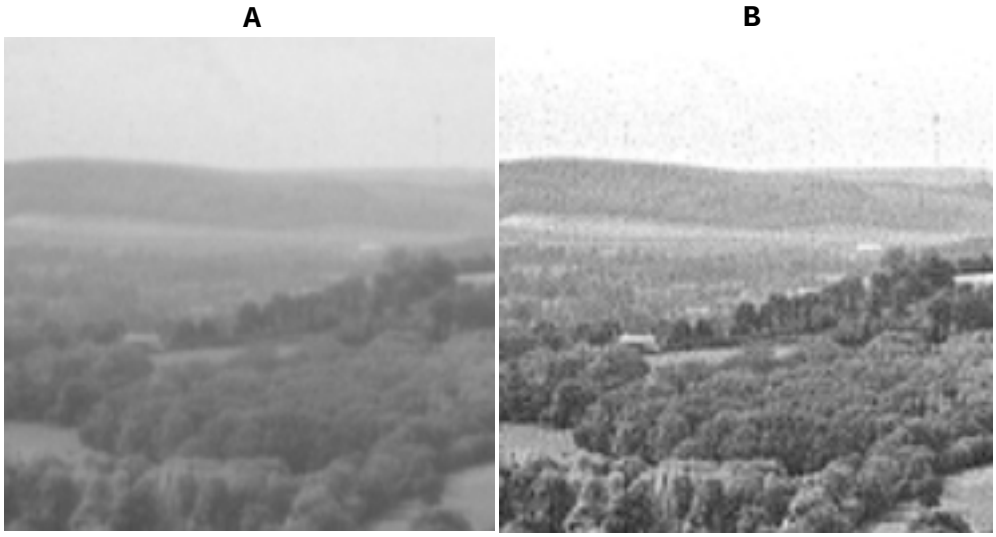

FIG. 9. *Extent of sharpening in the English village image becomes more evident with zooming. The enhanced image* (b) *shows buildings in the distance not immediately apparent in the original image* (a).

improvements visible in Figures 6 through 9. The "before and after" Fourier transform pattern shown in Figure 10(a) occurs in every example discussed in this paper, with the exception of the F15 image in Figure 12; the anomalous behavior in that case is shown in Figure 10(b).

The next example is the boat image in Figure 11(a). With $A = 4.0$, the APEX fit on $|\xi| \leq 250$ returned $\alpha = 0.518155$, $\beta = 0.215083$. Using these values in the SECB method, with $s = 0.01$, $K = 1300$, and continuation terminated at $t = 0.5$, produced

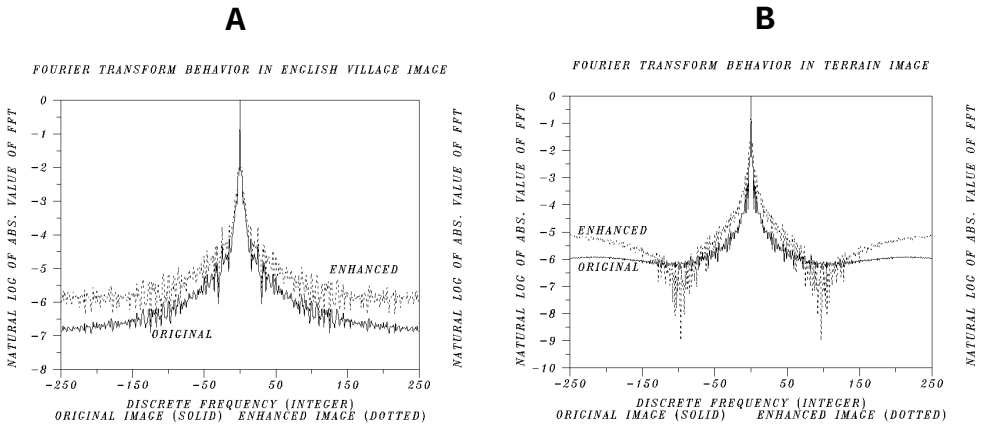

FIG. 10. *APEX processing significantly alters Fourier transform behavior.* (a) *English village image before and after processing.* (b) *F*15 *terrain image in Figure* 12 *before and after processing. The behavior shown in* (b) *is exceptional; all other examples in the present paper conform with the behavior shown in* (a).

FIG. 11. *Enhancement of the boat image. The APEX method with* $A = 4.0$ *on* $|\xi| \leq 250$ *yields* $\alpha = 0.518155$, $\beta = 0.215083$. *Using these parameters, with* $s = 0.01$, $K = 1300$, *and backwards continuation terminated at* $t = 0.5$, *the SECB method applied to image* (a) *produces image* (b). *The number* 7 2 7 *on the side of the boat in image* (b) *was not easily identifiable in image* (a).

Figure 11(b). Enhancement has now rendered visible the number 7 2 7 on the left side of the boat. Other identifiable details include the stripe along the left trouser leg of the man on the ground, the lettering on the sign hanging from the boat to his right, and part of the stone work and stairway to the left of the lighthouse.

The F15 plane image in Figure 12(a) is another interesting example. The aim here is to enhance the background terrain. With $A = 3.5$, the APEX fit on $|\xi| \leq 250$ develops a cusp at $\xi = 0$ and returns $\alpha = 0.856096$, $\beta = 0.107289$. Using these

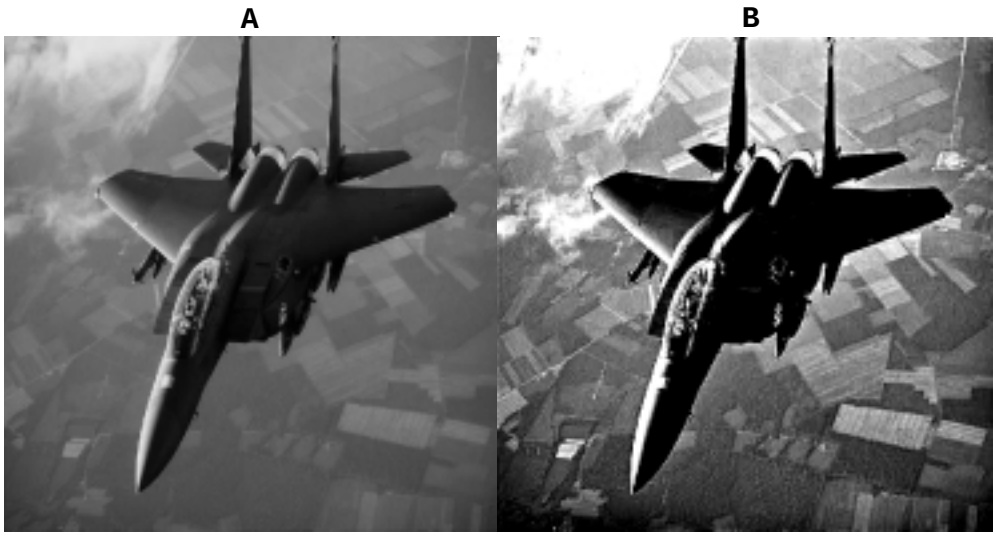

FIG. 12. *Striking enhancement of terrain features in an F*15 *image. The APEX method with* $A = 3.5$ *on* $|\xi| \leq 250$ *yields* $\alpha = 0.856096$, $\beta = 0.107289$. *Using these parameters, with* $s = 0.01$, $K = 1000$, *and backwards continuation terminated at* $t = 0.25$, *the SECB method applied to image* (a) *produced image* (b). *Condensation trails behind the aircraft in image* (b) *were not immediately evident in image* (a).

values in the SECB method, with $s = 0.01$, $K = 1000$, and backwards continuation terminated at $t = 0.25$, produces rather striking enhancement of the ground features in Figure 12(b). This example is noteworthy on two counts: the exceptionally low value of β detected by the APEX method and the previously mentioned unexpected Fourier behavior shown in Figure 10(b).

Beginning with Figure 1, all of the examples discussed so far involve images of familiar objects. This allows for relatively easy evaluation of the results of APEX processing. The next five examples involve less familiar objects. Moreover, fine details visible on a modern high resolution computer screen are sometimes lost in the printing process. Consequently, improvements in image quality in some of the next examples may seem less obvious than in previous examples. At the same time, the performance of the APEX method in reconstructing real details of familiar objects provides a measure of confidence in the results obtained when that method is applied to unfamiliar objects.

Figure 13(a) is a Landsat image of the Washington, DC area. With $A = 4.25$, the APEX fit on $|\xi| \leq 250$ returns $\alpha = 0.540825$, $\beta = 0.182410$. Using these parameters in the SECB method, with $s = 0.01$, $K = 1300$, and continuation terminated at $t = 0.5$, produces Figure 13(b). There is a significant increase in resolution in Figure 13(b), which improves definition of several landmarks and thoroughfares. The Washington Monument, the bridges over the Potomac, Pennsylvania and Maryland Avenues radiating from the Capitol, Massachusetts Avenue to the north, and Virginia Avenue and the Southeast Freeway to the south are some of the features that are more easily identified in the enhanced image.

Figure 14(a) is a scanning electron microscope image of a mosquito's head. A prominent feature is the insect's compound eye. With $A = 4.0$, the APEX fit on $|\xi| \leq 250$ yields $\alpha = 0.734259$, $\beta = 0.156963$. Using these values in the SECB method, with

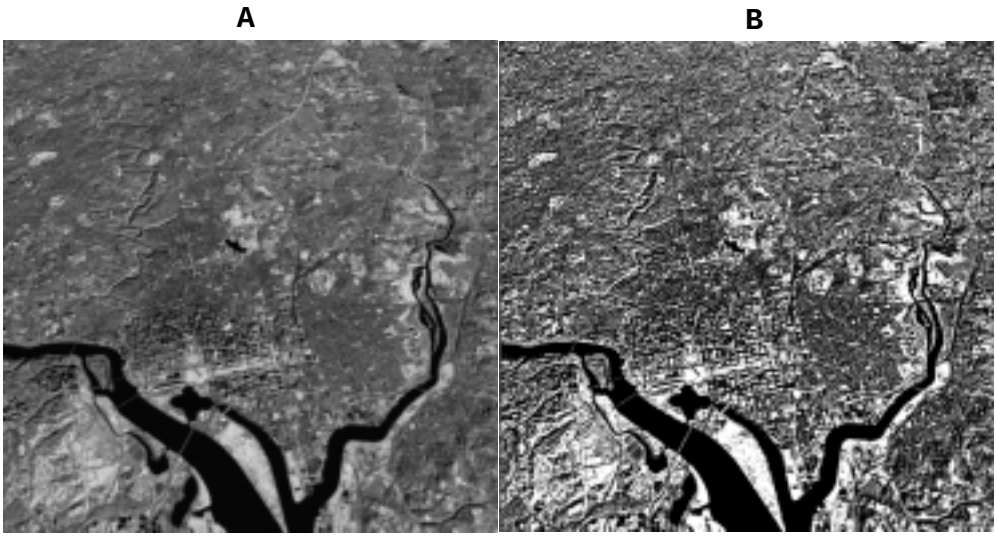

FIG. 13. *Enhancement of a Washington, DC Landsat image. The APEX method with* $A = 4.25$ *on* $|\xi| \leq 250$ *yields* $\alpha = 0.540825$, $\beta = 0.182410$. *Using these parameters, with* $s = 0.01$, $K = 1300$, *and backwards continuation terminated at* $t = 0.5$, *the SECB method applied to image* (a) *produced image* (b). *Increased resolution in image* (b) *improves definition of several landmarks and thoroughfares.*

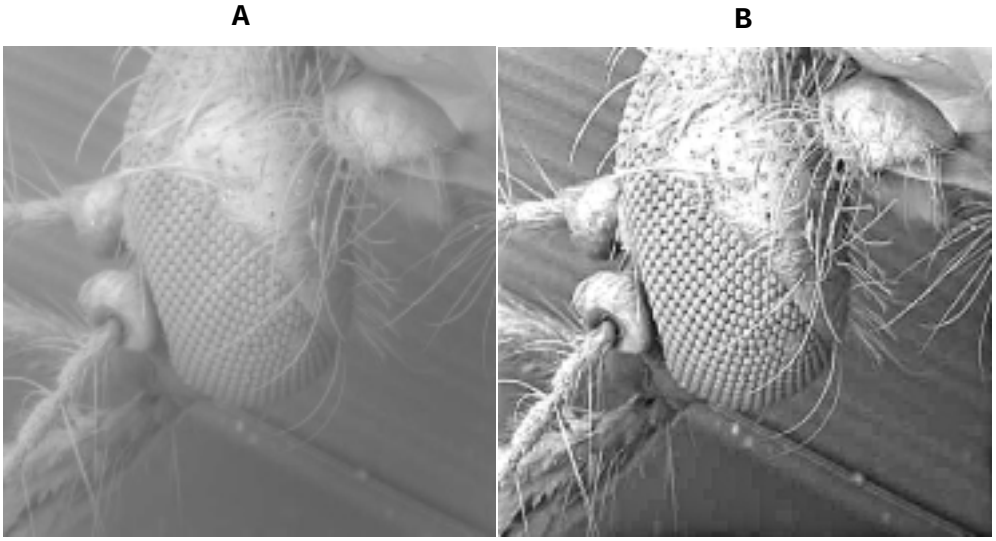

FIG. 14. *Enhancement of a scanning electron microscope image of a mosquito's head showing the compound eye. The APEX method with* $A = 4.0$ *on* $|\xi| \leq 250$ *yields* $\alpha = 0.734259$, $\beta = 0.156963$. *Using these parameters, with* $s = 0.001$, $K = 10$, *and backwards continuation terminated at* $t = 0.4$, *the SECB method applied to image* (a) *produced image* (b). *APEX processing enhances contrast and brings the eye into sharper focus. Further applications in electron microscopy are discussed in* [10].

$s = 0.001$, $K = 10.0$, and backwards continuation terminated at $t = 0.4$, produces Figure 14(b). Evidently, APEX processing results in significant overall improvement. In particular, the eye appears in much sharper focus. Further applications to electron

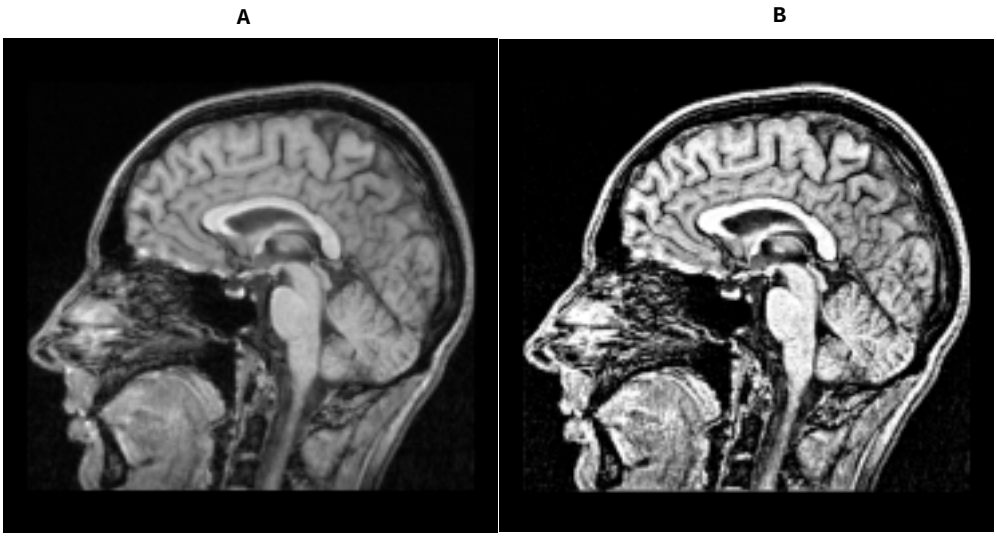

FIG. 15. *Enhancement of a sagittal MRI brain image. The APEX method with* $A = 4.0$ *on* $|\xi| \leq 250$ *yields* $\alpha = 0.333267$, $\beta = 0.209416$. *Using these parameters, with* $s = 0.01$, $K = 1300$, *and backwards continuation terminated at* $t = 0.35$, *the SECB procedure applied to image* (a) *produced image* (b). *APEX processing noticeably improves feature definition in areas between two and four o'clock.*

microscopy are discussed in [10].

The sagittal MRI (magnetic resonance imaging) brain image in Figure 15(a) has been used as a test *sharp* image in previous publications. In [5] and [7], synthetically blurred versions of that sharp image were used in a comparative evaluation of restoration algorithms when the psf is *known*. Here, we consider further sharpening the sharp image by blind deconvolution. With $A = 4.0$, the APEX fit on $|\xi| \leq 250$ returns $\alpha = 0.333267$, $\beta = 0.209416$. Using these parameters in the SECB procedure, with $s = 0.01$, $K = 1300$, and continuation terminated at $t = 0.35$, produced the image in Figure 15(b). Substantial improvement is apparent over the whole image. In the sector between two and four o'clock, in particular, sharpening of structural detail significantly improves feature definition.

In PET (positron emission tomography) imaging, a positron emitting radionuclide is injected into the patient and used to tag glucose molecules in their course through the brain. The metabolic rate of glucose is a key parameter that reflects cerebral function and indicates the extent to which regions of the brain are active. Performing specific mental tasks activates various parts of the brain, causing increased glucose uptake and hence increased positron emission. Centers of activity translate into relatively bright spots in the PET image. However, blurring by the scanner psf tends to average out such relative differences, resulting in loss of contrast. Figure 16(a) is a PET image of a transverse (horizontal) slice through the brain. Blind deconvolution is used to enhance that image. With $A = 5.0$, the APEX fit on $|\xi| \leq 250$ returns $\alpha = 0.198931$, $\beta = 0.284449$. Using these parameters in the SECB method, with $s = 0.001$, $K = 5.0$, and backwards continuation terminated at $t = 0.6$, produces Figure 16(b). Note that both images in Figure 16 show identical features, but the contrast has been increased in the APEX-processed image, with some regions becoming darker while others have become lighter. In particular, several bright spots appear

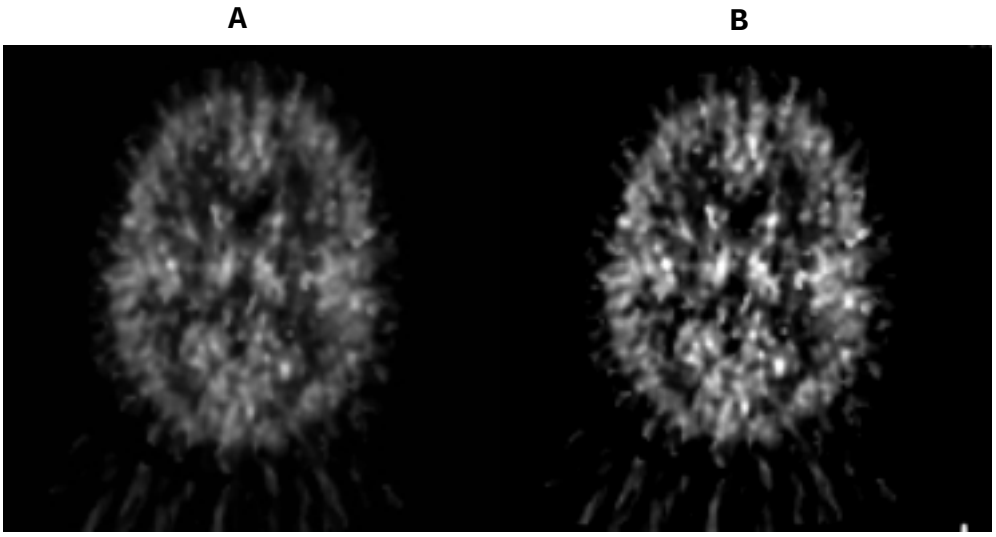

FIG. 16. *Enhancement of a transverse PET brain image. The APEX method with* $A = 5.0$ *on* $|\xi| \leq 250$ *yields* $\alpha = 0.198931$, $\beta = 0.284449$. *Using these parameters, with* $s = 0.001$, $K = 5.0$, *and backwards continuation terminated at* $t = 0.6$, *the SECB procedure applied to image* (a) *produced image* (b). *Bright spots in the enhanced image* (b), *indicating areas of the brain responding to applied external stimuli, are more clearly defined than in the original image* (a).

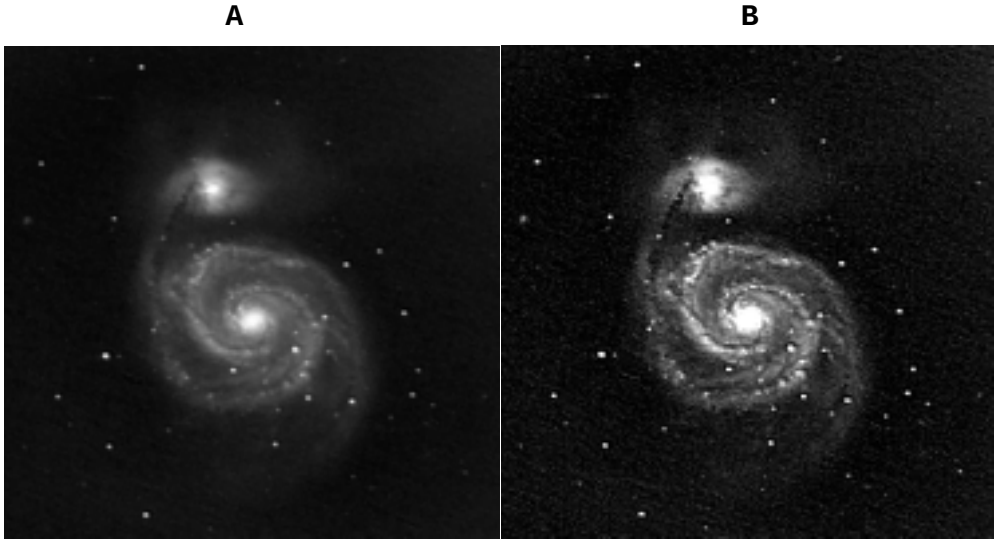

FIG. 17. *Enhancement of the Whirlpool galaxy (M*51*) image. The APEX method with* $A = 4.0$ *on* $|\xi| \leq 250$ *yields* $\alpha = 0.451615$, $\beta = 0.221955$. *Using these parameters, with* $s = 0.001$, $K = 5.0$, *and backwards continuation terminated at* $t = 0.5$, *the SECB applied to image* (a) *produced image* (b). *APEX processing increases resolution and enhances luminosity in the spiral arms and galactic cores.*

in Figure 16(b) that were not as readily apparent in the original image.

Our last example is the Whirlpool galaxy (M51) in Figure 17(a). With $A = 4.0$, the APEX fit on $|\xi| \leq 250$ yields $\alpha = 0.451615$, $\beta = 0.221955$. Using these values in

the SECB method, with $s = 0.001$, $K = 5.0$, and backwards continuation terminated at $t = 0.5$, produced Figure 17(b). In the enhanced image, the spiral arms are more luminous and better defined, and the luminous cores are larger in both the spiral galaxy and its companion. The dark connecting arm between the two galaxies is also more clearly defined. These enhancements are due to a change in Fourier transform behavior brought about by deconvolution with the APEX-detected psf. This change in Fourier behavior is similar to that shown in Figure 10(a), although it is more pronounced. A concomitant effect of deconvolution is amplification of data noise, which now becomes visible against the dark background in Figure 17(b).

Clearly, in this galaxy image as in the preceding PET image, there is no way of knowing whether the enhanced image conforms with reality. Conceivably, the increased luminosity in Figure 17(b) may be exaggerated. However, the bright areas along the galactic arms in Figure 17(b), as well as the bright spots in Figure 16(b), did not materialize spontaneously. These areas must have been just below some brightness threshold in the original image, and APEX processing has served the very useful purpose of revealing their presence. If such areas appear overenhanced, this can be corrected by repeating the SECB procedure and terminating continuation at *higher* values of t.

7. Anisotropic diffusion, total variation deblurring, and the "staircase effect." As is evident from the survey [11], there is considerable interest in the use of anisotropic diffusion equations to perform various tasks in image processing. In pure denoising applications, such methods have been found to be effective at removing high levels of noise while preserving edges in an image. An important related idea is the use of the *total variation* norm for regularizing the image restoration problem [12], [13], [16], [33], [37], [38]. The Euler–Lagrange problem for minimizing the total variation can be written as a nonlinear anisotropic diffusion equation, with a forcing term that describes convolution of the unknown image with the known psf. This is supplemented by homogeneous Neumann boundary conditions together with the blurred image as initial data; see [33]. Deblurring the image is equivalent to stepwise numerical computation of this nonlinear initial value problem until a steady state is reached.

Total variation deblurring is especially useful for recovering "blocky" images, i.e., images that are nearly piecewise constant and have many edges [12], [16]. For this reason, the total variation blind deconvolution approach in [13] aims primarily at recovering blocky images that had been blurred by psfs with *sharp edges*. This is the case with defocus and motion blurs; a defocused satellite image is the example used in [13]. The authors observe that their algorithm is more effective on defocused images than it is on Gaussian blurred images. In a complementary role, the APEX method can also handle blocky images, but it is based on detecting class **G** blurs, a class that includes heavy-tailed psfs but excludes defocus and motion blurs.

A major drawback of the total variation approach is the so-called "staircase effect," whereby the deblurred image can develop spurious piecewise constant regions. This often produces an "oil painting" appearance that does not correspond to the true image and prevents identification of fine detail. For this reason, the authors in [12] and [16] conclude that total variation deblurring is not useful for images that are not nearly piecewise constant. In [34], [35], it is proved that total variation restoration necessarily leads to the staircase effect. In [19], the mathematical premise of minimizing image total variation is questioned, and the authors prove that because of their fine texture, most natural images are *not* of bounded variation. Therefore, in images

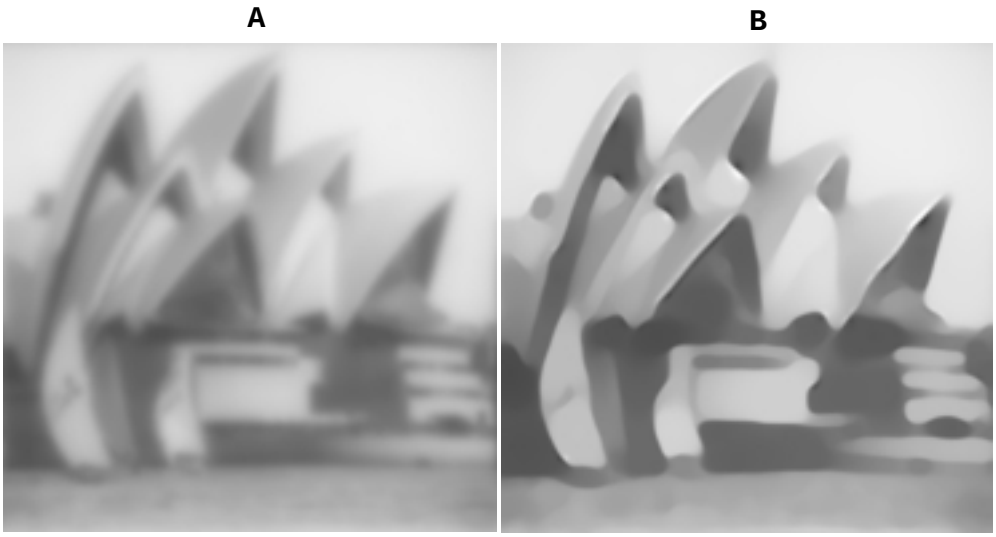

FIG. 18. *Staircase effect in total variation deblurring of the Sydney image.* (a) *Synthetically blurred* 512×512 *Sydney image, previously used in Figure* 1(b)*, was computed in* 64*-bit precision.* (b) *Deblurring of image* (a) *using the known psf and the total variation scheme in* [33]*, with noise variance parameter* $\beta^{\Sigma} = 0.001$*, Lagrange multiplier* $\lambda = 50$*, CFL restriction* $\Delta t = 0.1(\Delta x)^2$*, and stepwise integration to time* $T = 100\Delta t$*. The strong "oil painting" effect in image* (b) *impairs recognition and occurs with other choices of* $\beta^{\Sigma} \leq 0.001$ *and* $\lambda \geq 50$*. Compare with the SECB deblurred image in Figure* 1(c).

with fine texture, total variation deblurring must inevitably smooth out texture.

The following example illustrates why total variation deblurring is typically not useful for the type of textured imagery considered in this paper. The blurred noiseless 512×512 Sydney image, previously used in Figure 1(b), was deblurred using the total variation scheme described in [33, section 5]. This is a pure deblurring problem in which the synthetically blurred input image, Figure 18(a), was computed in 64-bit precision. Moreover, the precisely known psf was used. The aim here is to evaluate the reconstructive ability of the total variation scheme under the most favorable circumstances. As recommended in [33], in this noiseless case the noise variance parameter β^{Σ} should be chosen small, while the Lagrange multiplier λ should be chosen large. Here, several values of β^{Σ} in the range $0.00001 \leq \beta^{\Sigma} \leq 0.01$ were tried, together with several values of λ in the range $1 \leq \lambda \leq 100$. The CFL restriction $\Delta t = 0.1(\Delta x)^2$ was applied with all these choices, and no sign of computational instability was detected. Figure 18(b) is the result of stepwise numerical computation of the nonlinear diffusion problem in [33, section 5] up to time $T = 100\Delta t$, using $\beta^{\Sigma} = 0.001$ and $\lambda = 50$. The "oil painting" effect in Figure 18(b) occurs with other choices of $\beta^{\Sigma} \leq 0.001$ and $\lambda \geq 50$, and the deblurred image does not improve if more time steps are taken. SECB deblurring of the same image is shown in Figure 1(c). In the presence of noise, the SECB deblurred image is less sharp, but maintains its strong qualitative edge over Figure 18(b). It should be noted that the authors in [33] did not intend their scheme to be used for images as seriously blurred as Figure 18(a). However, the staircase effect is still pronounced, even with more mildly blurred images.

8. Concluding remarks. Setting aside all theoretical considerations, APEX processing is a practical enhancement technique that can sharpen significant classes

of images originating from diverse imaging modalities. One important feature of this approach is its fast implementation on desktop platforms. Even with large image sizes, numerous trial restorations can be accomplished in seconds or minutes of cpu time. This makes for easy fine tuning of parameters and a quick determination of whether the APEX method significantly improves a given image. Once improvement is detected, fine tuning must be used to obtain optimal results. Here, another important feature of the APEX method plays a useful role. This is the marching-backwards-in-time option characteristic of class **G** psfs, which allows for deconvolution to be performed in *slow motion*. Robustness is a third important property of the APEX method, allowing detection of multiple psfs capable of significant sharpening. This substantially increases the probability of finding a useful candidate.

On the theoretical side, this paper raises new questions. The first of these is the existence of several useful psfs, as demonstrated for the Sydney image in Figure 1. This phenomenon warrants further investigation. A second question concerns the important role Lévy psfs appear to play in numerous imaging systems. The discussion in section 2 has surveyed *inferences* of stable laws that have been made from mtf measurements. Development of methods of analyzing imaging systems that can rigorously establish such laws, and predict the Lévy exponent β, would be a major advance.

Reconciling the results of section 2 with the behavior of large classes of images raises additional questions. Electronic imaging psfs $h(x, y)$ are found to have Lévy exponents $\beta > 0.5$ in most cases, so that $\log \hat{h}(\xi, 0) = -\alpha|\xi|^{2\beta}$ is a monotone decreasing concave function on $\xi > 0$. However, as illustrated in Figure 3, all images $g(x, y)$ used in this paper are such that global behavior in $\log|\hat{g}^*(\xi, 0)|$ is generally monotone decreasing and *convex*. Another large class of images with this convexity property, the class **W**, was described in [9]. When such images are APEX-fitted with a Lévy psf in the manner shown in Figure 5(b), a value of $\beta \leq 0.5$ is inevitably detected. An average value of $\beta = 0.23$ was found for the six images in Figures 4, 6, 11, 15, 16, and 17, and significantly lower values were found for the three images in Figures 12, 13, and 14. A possible partial explanation for this discrepancy is provided by the Sydney experiment in Figure 1. There, the APEX method detected several useful psfs with values of β *smaller* than the value that was used to blur the image. The detected β-values in the above nine images may likewise underestimate the true imaging system β-values. An entirely different scenario may be that the APEX method provides generic low exponent Lévy psfs capable of enhancing a wide variety of images, independently of the imaging physics that created them. Other generic enhancement techniques have been used for some time in image processing (see [36, Chapter 10]). More recent approaches based on nonlinear diffusion equations are also intended as generic enhancement methods [11]. However, nonlinear methods generally require large numbers of iterations and may not be well suited for real-time processing of complex high resolution imagery.

Whatever may be the reasons behind it, the effectiveness of the APEX method on many types of images is undeniable, and the method is a useful addition to the image processing toolbox.

REFERENCES

[1] O. Barndorff-Nielsen, T. Mikosch, and S. Resnick, eds., *Lévy Processes—Theory and Applications*, Birkhäuser Boston, Cambridge, MA, 2001.

[2] J. Bertouin, *Lévy Processes*, Cambridge Tracts in Math. 121, Cambridge University Press, Cambridge, UK, 1998.
[3] L. M. Biberman and S. Nudelman, *Photoelectronic Imaging Devices*, Plenum Press, New York, 1971.
[4] P. Biler, G. Karch, and W. A. Woyczyński, *Multifractal and Lévy conservation laws*, C. R. Acad. Sci. Paris Sér. I Math., 330 (2000), pp. 343–348.
[5] A. S. Carasso, *Overcoming Hölder continuity in ill-posed continuation problems*, SIAM J. Numer. Anal., 31 (1994), pp. 1535–1557.
[6] A. S. Carasso, *Error bounds in nonsmooth image deblurring*, SIAM J. Math. Anal., 28 (1997), pp. 656–668.
[7] A. S. Carasso, *Linear and nonlinear image deblurring: A documented study*, SIAM J. Numer. Anal., 36 (1999), pp. 1659–1689.
[8] A. S. Carasso, *Logarithmic convexity and the "slow evolution" constraint in ill-posed initial value problems*, SIAM J. Math. Anal., 30 (1999), pp. 479–496.
[9] A. S. Carasso, *Direct blind deconvolution*, SIAM J. Appl. Math., 61 (2001), pp. 1980–2007.
[10] A. S. Carasso, D. S. Bright, and A. E. Vladár, *The APEX method and real-time blind deconvolution of scanning electron microscope imagery*, Optical Engineering, 41 (2002), pp. 2499–2514.
[11] V. Caselles, J. M. Morel, G. Sapiro, and A. Tannenbaum, eds., *Special Issue on Partial Differential Equations and Geometry-Driven Diffusion in Image Processing*, IEEE Trans. Image Process., 7 (1998).
[12] A. Chambolle and P. L. Lions, *Image recovery via total variation minimization and related problems*, Numer. Math., 76 (1997), pp. 167–188.
[13] T. F. Chan and C. K. Wong, *Total variation blind deconvolution*, IEEE Trans. Image Process., 7 (1998), pp. 370–375.
[14] I. P. Csorba, ed., *Electron Image Tubes and Image Intensifiers*, Proc. SPIE 1243, 1990.
[15] I. P. Csorba, ed., *Electron Image Tubes and Image Intensifiers* II, Proc. SPIE 1449, 1991.
[16] D. C. Dobson and F. Santosa, *Recovery of blocky images from noisy and blurred data*, SIAM J. Appl. Math., 56 (1996), pp. 1181–1198.
[17] W. Feller, *An Introduction to Probability Theory and Its Applications*, Vol. 2, 2nd ed., Wiley, New York, 1971.
[18] R. E. Franseen and D. K. Schroder, eds., *Applications of Electronic Imaging Systems*, Proc. SPIE 143, 1978.
[19] Y. Gousseau and J.-M. Morel, *Are natural images of bounded variation?*, SIAM J. Math. Anal., 33 (2001), pp. 634–648.
[20] A. Heckert and J. J. Filliben, *DATAPLOT Reference Manual*, http://www.itl.nist.gov/div898/software/dataplot/document.htm.
[21] R. E. Hufnagel and N. R. Stanley, *Modulation transfer function associated with image transmission through turbulent media*, J. Opt. Soc. Amer., 54 (1964), pp. 52–61.
[22] C. B. Johnson, *A method for characterizing electro-optical device modulation transfer functions*, Photographic Science and Engineering, 14 (1970), pp. 413–415.
[23] C. B. Johnson, C. E. Catchpole, and C. C. Matle, *Microchannel plate inverter image intensifiers*, IEEE Trans. Electron Devices, 18 (1971), pp. 1113–1116.
[24] C. B. Johnson, *Classification of electron-optical device modulation transfer function*, Adv. Electronics and Electron Phys., 33B (1972), pp. 579–584.
[25] C. B. Johnson, *Circular aperture diffraction limited MTF: Approximate expressions*, Applied Optics, 11 (1972), pp. 1875–1876.
[26] C. B. Johnson, *MTFs: A simplified approach*, Electro-Optical Systems Design, 4 (1972), pp. 22–26.
[27] C. B. Johnson, *Point-spread functions, line-spread functions, and edge-response functions associated with mtfs of the form* $exp[-(\omega/\omega_c)^n]$, Applied Optics, 12 (1973), pp. 1031–1033.
[28] C. B. Johnson, *A convenient form of graph paper for determination of electro-optical device modulation transfer function parameters*, IEEE Trans. Electron Devices, 20 (1973), pp. 80–81.
[29] C. B. Johnson, *MTF parameters for all photographic films listed in Kodak pamphlet P-49*, Applied Optics, 15 (1976), p. 1130.
[30] C. B. Johnson, S. B. Patton, and E. Bender, *High-resolution microchannel plate image tube development*, in Proc. SPIE 1449, 1991, pp. 2–12.
[31] C. B. Johnson and B. N. Laprade, eds., *Electron Tubes and Image Intensifiers*, Proc. SPIE 1655, 1992.
[32] R. Kuske and J. B. Keller, *Rate of convergence to a stable law*, SIAM J. Appl. Math., 61 (2000), pp. 1308–1323.

[33] A. Marquina and S. Osher, *Explicit algorithms for a new time dependent model based on level set motion for nonlinear deblurring and noise removal*, SIAM J. Sci. Comput., 22 (2000), pp. 387–405.
[34] M. Nikolova, *Local strong homogeneity of a regularized estimator*, SIAM J. Appl. Math., 61 (2001), pp. 633–658.
[35] M. Nikolova, *Image restoration by minimizing objective functions with nonsmooth data-fidelity terms*, in Proceedings of the IEEE Workshop on Variational and Level Set Methods (VLSM01), International Conference on Computer Vision (ICCV 2001), Vancouver, IEEE, Piscataway, NJ, 2001.
[36] W. K. Pratt, *Digital Image Processing*, 2nd ed., Wiley, New York, 1991.
[37] L. Rudin and S. Osher, *Total variation based image restoration with free local constraints*, in Proceedings of the IEEE International Conference on Image Processing, Austin, TX, 1994, Vol. 1, pp. 31–35.
[38] L. Rudin, S. Osher, and E. Fatemi, *Nonlinear total variation based noise removal algorithms*, Phys. D, 60 (1992), pp. 259–268.
[39] G. Samorodnitsky and M. S. Taqqu, *Stable Non-Gaussian Random Processes: Stochastic Models with Infinite Variance*, Chapman and Hall, New York, 1994.
[40] M. F. Shlesinger, G. M. Zaslavsky, and U. Frisch, eds., *Lévy Flights and Related Topics in Physics*, Lecture Notes in Phys. 450, Springer-Verlag, New York, 1995.
[41] C. Tsallis, S. V. Levy, A. M. Souza, and R. Maynard, *Statistical-mechanical foundation of the ubiquity of Lévy distributions in nature*, Phys. Rev. Lett., 75 (1995), pp. 3589–3593.
[42] R. Weber, *The ground-based electro-optical detection of deep-space satellites*, in Proc. SPIE 143, 1978, pp. 59–69.
[43] C. S. Williams and O. A. Becklund, *Introduction to the Optical Transfer Function*, Wiley, New York, 1989.
[44] W. A. Woyczyński, *Lévy processes in the physical sciences*, in Lévy Processes—Theory and Applications, O. Barndorff-Nielsen, T. Mikosch, and S. Resnick, eds., Birkhäuser Boston, Cambridge, MA, 2001.